

## *Supporting Information*

# **Substituents Lead to Differences in the Formation of a Series of Dysprosium Hydrogen-Bonded Organic Frameworks with High Stability and Acid Stimulus–Response Luminescence Properties**

Jin-Mei Peng,<sup>†</sup> Hai-Ling Wang,<sup>†</sup> Zhong-Hong Zhu,<sup>†,‡,\*</sup> Zi-Yuan Liu,<sup>†</sup> Hua-Hong Zou,<sup>†,\*</sup> Fu-Pei Liang<sup>†,!,\*</sup>

<sup>†</sup>State Key Laboratory for Chemistry and Molecular Engineering of Medicinal Resources, School of Chemistry and Pharmacy of Guangxi Normal University, Guilin 541004, P. R. China

<sup>‡</sup>State Key Laboratory of Luminescent Materials and Devices, School of Materials Science and Engineering, South China University of Technology, 510640 Guangzhou, China

<sup>!</sup>Guangxi Key Laboratory of Electrochemical and Magnetochemical Functional Materials, College of Chemistry and Bioengineering, Guilin University of Technology, Guilin 541004, P. R. China

\*E-mail (Corresponding author): 18317725515@163.com (Z.-H. Zhu), gxnuchem@foxmail.com (H.-H. Zou), fliangoffice@yahoo.com (F.-P. Liang).

## Table of Contents:

<b>Supporting Tables</b>	
<b>Table S1</b>	Crystallographic data of the complexes <b>1-5</b> .
<b>Table S2</b>	<a href="#">Crystallographic data of the complexes <b>1a</b>.</a>
<b>Table S3</b>	Selected bond lengths (Å) and angles (°) of complexes <b>1-5</b> .
<b>Table S4</b>	<a href="#">Selected bond lengths (Å) and angles (°) of complexes <b>1a</b>.</a>
<b>Table S5-S9</b>	<i>SHAPE</i> analysis of the Dy <sup>III</sup> ion in <b>1-5</b> .
<b>Table S10</b>	Operating conditions for elemental analysis to use ICP-OES.
<b>Table S11</b>	<a href="#">Analytical features of ICP-OES to determine whether Pb(II) ions are entered in the <b>1a</b> frame in response to Pb(II) ions.</a>
<b>Table S12-S14</b>	Selected parameters from the fitting result of the Cole-Cole plots for <b>1-5</b> under 0 Oe field.
<b>Supporting Figures</b>	
<b>Figure S1</b>	Two different coordination modes of Schiff base ligand in the independent unit of <b>1</b> .
<b>Figure S2</b>	The coordination polyhedrons around Dy <sup>III</sup> ions in complexes <b>2-5</b> .
<b>Figure S3</b>	a) Weak interaction of C–H···π (Ph) between molecules at a direction, a) for <b>2</b> , b) for <b>3</b> , c) for <b>4</b> .
<b>Figure S4</b>	Crystal structure of <b>5</b> , a) 1D chain; b) 2D layer; c) 3D supramolecular framework.
<b>Figure S5</b>	IR spectra of <b>1</b> (red), <b>2</b> (brown), <b>3</b> (green), <b>4</b> (blue), and <b>5</b> (purple).
<b>Figure S6</b>	Theoretical and experimental PXRD patterns of Dy-HOFs ( <b>1-5</b> ).
<b>Figure S7</b>	<a href="#">Theoretical PXRD patterns of <b>1</b> and <b>1a</b>.</a>
<b>Figure S8</b>	Thermogravimetric curves of complexes <b>1-5</b> (a-e, TG and DTG).
<b>Figure S9</b>	Thermogravimetric curve of solvent exchange for complex <b>1</b> (a for CH <sub>3</sub> OH, b for C <sub>2</sub> H <sub>5</sub> OH, c for CH <sub>3</sub> CN)
<b>Figure S10</b>	N <sub>2</sub> adsorption and desorption isotherms of <b>1</b> at 77 K.
<b>Figure S11</b>	Photos of the sample <b>1</b> immersed in HCl aqueous solution and original sample seen under the radiation of 365 nm UV lamp.
<b>Figure S12</b>	a) The UV-Vis absorption spectra of <b>1</b> , <b>4</b> and <b>5</b> ; Solid-state fluorescence of complexes <b>4</b> (b) and <b>5</b> (c).
<b>Figure S13</b>	The pH stimuli-response luminescence intensity with a) $\lambda_{\text{ex}} = 429$ nm for <b>1</b> , b) $\lambda_{\text{ex}} = 440$ nm for <b>4</b> , c) $\lambda_{\text{ex}} = 458$ nm for <b>5</b> .
<b>Figure S14</b>	a) Mass spectrometry analysis of the sample <b>1a</b> responding to Zn <sup>2+</sup> ; b) Theoretical and experimental PXRD patterns of the sample <b>1a</b> responding to metal ion.
<b>Figure S15</b>	UV absorption of sample <b>1a</b> to aqueous solutions containing Pb(II) ions of different concentrations.
<b>Figure S16</b>	Untreated <i>HeLa</i> cells as a blank control group (a for <b>1</b> , d for <b>5</b> ); At 429 nm, the state of <i>HeLa</i> cells after adding sample <b>1</b> (b), and sample <b>1</b> which was soaked in HCl (c); At 458 nm, the state of <i>HeLa</i> cells after adding sample <b>5</b> (e), and sample <b>5</b> which was soaked in HCl (f) (scale: 100 μm).
<b>Figure S17</b>	Fluorescence of the DMSO solution of <b>1</b> in a simulated environment
<b>Figure S18</b>	Temperature dependence of $\chi_m T$ for <b>1-5</b> .

<b>Figure S19</b>	$M$ vs. $H$ plots for <b>1</b> (a), <b>2</b> (b), <b>3</b> (e), <b>4</b> (c), <b>5</b> (d). 2 K, green line; 2.5 K, blue line; 3 K, red line.
<b>Figure S20</b>	Temperature-dependent $\chi'$ and $\chi''$ AC susceptibilities under 0 DC field for <b>1</b> (a), <b>2</b> (b), <b>3</b> (c), <b>4</b> (d), <b>5</b> (e).
<b>Figure S21</b>	In phase ( $\chi'$ ) magnetic susceptibility vs frequency data under 0 DC field for <b>1</b> (a), <b>2</b> (b), <b>3</b> (c), <b>4</b> (d), and <b>5</b> (e).
<b>Figure S22</b>	Cole-Cole plots for <b>1</b> (a), <b>2</b> (b), <b>3</b> (c), <b>4</b> (d), and <b>5</b> (e), solid lines are the best fits to the Debye model.
<b>Figure S23</b>	$\ln(\tau)$ vs. $T^{-1}$ plots for <b>1</b> (a), <b>2</b> (b), <b>3</b> (c), <b>4</b> (d), and <b>5</b> (e), the solid lines show the best fits with the Arrhenius formula (linear) and the multiple relaxation processes equation (curve).

## Experimental section

### Synthesis of 1-5.

$[\text{Dy}(\text{L}^{1-\text{H}})(\text{L}^{2-\text{H}})]_n$  ( $\text{HL}^{1-\text{H}} = (\text{Z})\text{-2-}(((3\text{-amino-2,2-dimethylpropyl})\text{imino})\text{methyl})\text{phenol}$ ,  $\text{H}_2\text{L}^{2-\text{H}} = 2,2'\text{-}((1E,1'E)\text{-}((2,2\text{-dimethylpropane-1,3-diyl})\text{bis}(\text{azaneylylidene}))\text{bis}(\text{methaneylylidene}))\text{diphenol}$ ) (**1**). 2-hydroxybenzaldehyde (0.2 mmol), 2,2-dimethylpropane-1,3-diamine (0.1 mmol),  $\text{DyCl}_3 \cdot 6\text{H}_2\text{O}$  (0.2 mmol), EtOH (2 mL) and  $\text{Et}_3\text{N}$  (60  $\mu\text{L}$ ) were added to a Pyrex tube. The tube was frozen using liquid  $\text{N}_2$ , evacuated under vacuum and flame-sealed. Two hours latter, yellow crystal was precipitated at room temperature. The yield of **1** is 59.8% (based on  $\text{DyCl}_3 \cdot 6\text{H}_2\text{O}$ ). *Anal. Calc (%)*. for  $\text{C}_{31}\text{H}_{37}\text{DyN}_4\text{O}_3$ : C, 55.07; H, 5.52; N, 8.29; Found: C, 54.98; H, 5.46; N, 8.21. IR data (KBr,  $\text{cm}^{-1}$ ): 1623(s), 1472(s), 1330(s), 756(s), 3436(m), 2960(m), 1541(m), 3290(w), 2842(w), 1150(w), 799(w), 594(w).

$[\text{Dy}(\text{L}^{1-\text{Cl}})(\text{L}^{2-\text{Cl}})]_n$  ( $\text{HL}^{1-\text{Cl}} = (\text{Z})\text{-2-}(((3\text{-amino-2,2-dimethylpropyl})\text{imino})\text{methyl})\text{-4-chlorophenol}$ ,  $\text{H}_2\text{L}^{2-\text{Cl}} = 2,2'\text{-}((1E,1'E)\text{-}((2,2\text{-dimethylpropane-1,3-diyl})\text{bis}(\text{azaneylylidene}))\text{bis}(\text{methaneylylidene}))\text{bis}(4\text{-chlorophenol})$ ) (**2**). The procedure was similar to that of **1**, except that 5-chloro-2-hydroxybenzaldehyde was used instead of 2-hydroxybenzaldehyde. The yield of **2** is 63.7% (based on  $\text{DyCl}_3 \cdot 6\text{H}_2\text{O}$ ). *Anal. Calc (%)*. for  $\text{C}_{31}\text{H}_{34}\text{DyCl}_3\text{N}_4\text{O}_3$ : C, 47.77; H, 4.40; N, 7.19; Found: C, 47.71; H, 4.29; N, 7.12. IR data (KBr,  $\text{cm}^{-1}$ ): 1625(s), 1471(s), 827(s), 720(s), 3432(m), 1531(m), 1387(m), 1323(m), 663(m), 2957(w), 1176(w), 1061(w), 894(w).

$[\text{Dy}(\text{L}^{1-\text{Br}})(\text{L}^{2-\text{Br}})]_n$  ( $\text{HL}^{1-\text{Br}} = (\text{Z})\text{-2-}(((3\text{-amino-2,2-dimethylpropyl})\text{imino})\text{methyl})\text{-4-bromophenol}$ ,  $\text{H}_2\text{L}^{2-\text{Br}} = 2,2'\text{-}((1E,1'E)\text{-}((2,2\text{-dimethylpropane-1,3-diyl})\text{bis}(\text{azaneylylidene}))\text{bis}(\text{methaneylylidene}))\text{bis}(4\text{-bromophenol})$ ) (**3**). The procedure was similar to that of **1**, except that 5-bromo-2-hydroxybenzaldehyde was used instead of 2-hydroxybenzaldehyde. The yield of **3** is 63.7% (based on  $\text{DyCl}_3 \cdot 6\text{H}_2\text{O}$ ). *Anal. Calc (%)*. for  $\text{C}_{31}\text{H}_{34}\text{DyCl}_3\text{N}_4\text{O}_3$ : C, 47.77; H, 4.40; N, 7.19; Found: C, 47.71; H, 4.29; N, 7.12. IR data (KBr,  $\text{cm}^{-1}$ ): 1625(s), 1471(s), 827(s), 720(s), 3432(m), 1531(m), 1387(m), 1323(m), 663(m), 2957(w), 1176(w), 1061(w), 894(w).

diyl)bis(azaneylylidene))bis(methaneylylidene))bis(4-bromophenol) (**3**). The procedure was similar to that of **1**, except that 5-bromo-2-hydroxybenzaldehyde was used instead of 2-hydroxybenzaldehyde. The yield of **3** is 60.6% (based on  $\text{DyCl}_3 \cdot 6\text{H}_2\text{O}$ ). *Anal. Calc (%)*. for  $\text{C}_{31}\text{H}_{34}\text{DyBr}_3\text{N}_4\text{O}_3$ : C, 40.79; H, 3.75; N, 6.14; Found: C, 40.68; H, 3.63; N, 6.09. IR data (KBr,  $\text{cm}^{-1}$ ): 1623(s), 1470(s), 3432(m), 1385(m), 1322(m), 826(m), 2957(w), 1528(m), 1174(m), 961(w), 806(w), 639(w).

$[\text{Dy}(\text{L}^{1-\text{CH}_3})(\text{L}^{2-\text{CH}_3})]_n \quad \text{HL}^{1-\text{CH}_3} = (\text{Z})\text{-2-}((\text{3-amino-2,2-dimethylpropyl})\text{imino})\text{methyl}\text{-4-methylphenol},$   $\text{H}_2\text{L}^{2-\text{CH}_3} = 2,2'\text{-}((1E,1'E)\text{-}((2,2\text{-dimethylpropane-1,3-diyl})\text{bis(azaneylylidene)})\text{bis(methaneylylidene)})\text{bis(4-methylphenol)} (\mathbf{4})$ . The procedure was similar to that of **1**, except that 2-hydroxy-5-methoxybenzaldehyde was used instead of 2-hydroxybenzaldehyde. The yield of **4** is 58.3% (based on  $\text{DyCl}_3 \cdot 6\text{H}_2\text{O}$ ). *Anal. Calc (%)*. for  $\text{C}_{34}\text{H}_{43}\text{DyN}_4\text{O}_3$ : C, 56.86; H, 6.03; N, 7.80; Found: C, 56.77; H, 5.93; N, 7.72. IR data (KBr,  $\text{cm}^{-1}$ ): 1625(s), 1482(s), 1419(s), 824(s), 3437(m), 1540(m), 3437(m), 824(m), 2956(w), 1159(w), 1064(w), 501(w).

$[\text{Dy}(\text{L}^{1-\text{F}})(\text{L}^{2-\text{F}})]_n \quad \text{HL}^{1-\text{F}} = (\text{Z})\text{-2-}((\text{3-amino-2,2-dimethylpropyl})\text{imino})\text{methyl}\text{-4-fluorophenol},$   $\text{H}_2\text{L}^{2-\text{F}} = 2,2'\text{-}((1E,1'E)\text{-}((2,2\text{-dimethylpropane-1,3-diyl})\text{bis(azaneylylidene)})\text{bis(methaneylylidene)})\text{bis(4-fluorophenol)} (\mathbf{5})$ . The procedure was similar to that of **1**, except that 5-fluoro-2-hydroxybenzaldehyde was used instead of 2-hydroxybenzaldehyde. The yield of **5** is 60.9% (based on  $\text{DyCl}_3 \cdot 6\text{H}_2\text{O}$ ). *Anal. Calc (%)*. for  $\text{C}_{31}\text{H}_{34}\text{DyF}_3\text{N}_4\text{O}_{33}$ : C, 30.79; H, 2.83; N, 4.63; Found: C, 30.65; H, 2.67; N, 4.58. IR data (KBr,  $\text{cm}^{-1}$ ): 1627(s), 1474(s), 815(s), 1548(m), 3434(m), 1391(m), 1318(m), 1243(m), 1141(m), 2957(w), 1050(w), 579(w).

## Materials and Measurements.

All reagents are obtained from commercial sources and can be used without further purification. Elemental analysis (C, H, N) was measured on an Elementar Micro cube elemental analyzer. Thermal analysis was performed in  $\text{N}_2$  at a heating rate of 5  $^{\circ}\text{C}/\text{min}$  using Labsys Evo TG-DTG/DSC. IR spectra with KBr pellets were recorded on PE Spectrum Two FT/IR spectrometer (400–4,000  $\text{cm}^{-1}$ ). PXRD measurements were recorded on Rigaku D/max-III A diffractometer. Measurements of magnetic susceptibility were carried out within the temperature range of 2–300 K

using a Quantum Design MPMS SQUID-XL magnetometer equipped with a 5 T magnet. The diamagnetic corrections for these complexes were estimated using Pascal's constants, and magnetic data were corrected for diamagnetic contributions of the sample holder. Alternating current susceptibility measurements were performed from powdered samples to determine the in-phase and out-of-phase components of the magnetic susceptibility. The data were collected by increasing the temperature from 2 K to 15 K within frequencies ranging from 10 to 1,000 Hz, with no applied external dc field and a drive frequency of 2 Oe. In the samples where free movement of crystallites was prevented, silicone grease was employed for embedding.

### **Single-crystal X-ray crystallography.**

Diffraction data for all complexes were measured on a Bruker SMART CCD diffractometer (Mo-K $\alpha$  radiation and  $\lambda = 0.71073 \text{ \AA}$ ) in  $\Phi$  and  $\omega$  scan modes. All structures were solved by direct methods, followed by difference Fourier syntheses, and then refined by full-matrix least-squares techniques on  $F^2$  using *SHELXL*. All other non-hydrogen atoms were refined with anisotropic thermal parameters. Hydrogen atoms were placed in the calculated position and refined in the isotropic direction using a riding model. Table S1 and Table S2 summarizes X-ray crystallographic data and refinement details for the complexes. The CCDC reference numbers are 2044444–2044448 and 2088488 for Dy-HOFs (**1–5**) and **1a**.

### **Preparation of acid soaked samples and solid state fluorescence test.**

We prepare HCl aqueous solutions with pH = 1–6 respectively, and then divide 3 mL into 5 mL sample tubes. Weigh 5 mg of sample **1** and add to the sample tubes containing HCl aqueous solutions with different pH to soak. After 24 hours, filter and take out. Let it dry naturally for 2 h (named sample **1a**). Placing the dry sample under an ultraviolet lamp to observe and perform a solid-state fluorescence test. The test condition is that the slit width is set to 5 nm, the scanning speed is 240 nm/min, the scanning voltage is 490 eV at room temperature. Similarly, the acid immersion samples of samples **4** and **5** (**4a** and **5a**) and the test are the same as **1**.

### **Experiments in simulating standard physiological environments and acidic tumor**

**microenvironments.**

Firstly, an aqueous solution with pH = 7.3 in the simulated standard physiological environment (A) and an aqueous solution with pH = 5.4 in the simulated acidic tumor microenvironment (B) were prepared respectively. Then, 20  $\mu\text{mol/L}$  DMSO solution of **1** was added to the above two systems. Finally, their fluorescence was tested.

**Table S1.** Crystallographic data of the complexes **1-5**.

Complex	<b>1</b>	<b>2</b>	<b>3</b>	<b>4</b>	<b>5</b>
Formula	$\text{C}_{31}\text{H}_{37}\text{DyN}_4\text{O}_3$	$\text{C}_{31}\text{H}_{34}\text{DyCl}_3\text{N}_4\text{O}_3$	$\text{C}_{31}\text{H}_{34}\text{DyBr}_3\text{N}_4\text{O}_3$	$\text{C}_{34}\text{H}_{43}\text{DyN}_4\text{O}_3$	$\text{C}_{31}\text{H}_{34}\text{DyF}_3\text{N}_4\text{O}_3$
Formula weight	676.14	780.48	912.85	718.22	730.12
<i>T</i> (K)	293(2)	293(2)	293(2)	293(2)	293(2)
Crystal system	Triclinic	Triclinic	Triclinic	Triclinic	Monoclinic
Space group	<i>P</i> -1	<i>P</i> -1	<i>P</i> -1	<i>P</i> -1	<i>P</i> 2 <sub>1</sub> /c
<i>a</i> ( $\text{\AA}$ )	10.8652 (4)	11.4692(5)	11.4423(6)	11.1259(12)	12.1817(3)
<i>b</i> ( $\text{\AA}$ )	11.7883 (4)	11.6044(5)	11.9094(6)	11.5727(12)	20.5625(4)
<i>c</i> ( $\text{\AA}$ )	13.6002 (6)	13.4774(5)	13.4676(6)	13.3782(15)	12.7752(4)
$\alpha$ ( $^\circ$ )	113.151 (4)	79.557(3)	79.372(4) $^\circ$	83.724(9)	90
$\beta$ ( $^\circ$ )	105.580 (4)	69.062(4)	68.592(4) $^\circ$	81.585(9) $^\circ$	108.824(3)
$\gamma$ ( $^\circ$ )	98.522 (3)	73.811(4)	74.054(4) $^\circ$	78.314(9) $^\circ$	90
<i>V</i> ( $\text{\AA}^3$ )	1478.12 (11)	1602.21(12)	1635.60(15)	1663.0(3)	3028.86(14)
<i>Z</i>	2	2	2	2	4
<i>D</i> <sub>c</sub> ( $\text{g cm}^{-3}$ )	1.519	1.618	1.854	1.434	1.601
$\mu$ ( $\text{mm}^{-1}$ )	2.57	2.620	5.986	2.284	2.523
Reflns coll	19598	21440	21626	22031	20041
Unique reflns	6953	7558	7693	7734	7069
R <sub>int</sub>	0.0361	0.0394	0.0391	0.0776	0.0380

<sup>a</sup> $R_1[I \geq 2\sigma(I)]$	0.0309	0.0384	0.0396	0.0491	0.0323
<sup>b</sup> $wR_2(\text{all data})$	0.0688	0.0839	0.0831	0.0838	0.0702
GOF	1.068	1.059	1.039	1.013	1.087

$$^a R_1 = \sum ||F_o| - |F_c|| / \sum |F_o|, ^b wR_2 = [\sum w(F_o^2 - F_c^2)^2 / \sum w(F_o^2)^2]^{1/2}$$

**Table S2.** Crystallographic data of the complex **1a**.

Complex	<b>1a</b>
Formula	C <sub>31</sub> H <sub>37</sub> DyN <sub>4</sub> O <sub>3</sub>
Formula weight	676.14
T (K)	293(2)
Crystal system	Triclinic
Space group	P-1
<i>a</i> (Å)	10.8583 (5)
<i>b</i> (Å)	11.7999 (4)
<i>c</i> (Å)	13.6050 (5)
$\alpha$ (°)	113.197 (4)
$\beta$ (°)	105.551 (4)
$\gamma$ (°)	98.574 (3)
<i>V</i> (Å <sup>3</sup> )	1478.36 (11)
Z	2
<i>D<sub>c</sub></i> (g cm <sup>-3</sup> )	1.519
$\mu$ (mm <sup>-1</sup> )	2.56
Reflns coll	22779
Unique reflns	7006
R <sub>int</sub>	0.0413
<sup>a</sup> $R_1[I \geq 2\sigma(I)]$	0.0293
<sup>b</sup> $wR_2(\text{all data})$	0.0581

GOF	1.058
<sup>a</sup> R <sub>1</sub> = Σ  F <sub>o</sub>  - F <sub>c</sub>   /Σ F <sub>o</sub>  , <sup>b</sup> wR <sub>2</sub> = [Σw(F <sub>o</sub> <sup>2</sup> -F <sub>c</sub> <sup>2</sup> ) <sup>2</sup> /Σw(F <sub>o</sub> <sup>2</sup> ) <sup>2</sup> ] <sup>1/2</sup>	

**Table S3.** Selected bond lengths (Å) and angles (°) of complexes **1-5**.

1					
<b>Bond lengths (Å)</b>					
Dy1—O3	2.180 (2)	Dy1—O1	2.207 (2)	Dy1—O2	2.216 (2)
Dy1—N1	2.499 (3)	Dy1—N2	2.508 (3)	Dy1—N3	2.482 (3)
Dy1—N4	2.497 (3)				
<b>Bond angles (°)</b>					
O3—Dy1—O1	163.64 (9)	O3—Dy1—O2	90.45 (9)	O3—Dy1—N1	87.34 (9)
O3—Dy1—N2	92.73 (9)	O3—Dy1—N3	73.58 (9)	O1—Dy1—O2	105.84 (9)
O1—Dy1—N1	95.05 (9)	O1—Dy1—N2	73.19 (8)	O1—Dy1—N3	95.06 (9)
O1—Dy1—N4	80.70 (9)	O2—Dy1—N1	75.83 (8)	O2—Dy1—N2	144.52 (8)
O2—Dy1—N3	135.65 (8)	O2—Dy1—N4	73.72 (8)	N1—Dy1—N2	69.04 (8)
N3—Dy1—N1	141.54 (9)	N3—Dy1—N2	78.67 (8)	N3—Dy1—N4	71.66 (9)
N4—Dy1—N1	146.70 (9)	N4—Dy1—N2	138.20 (8)		
2					
<b>Bond lengths (Å)</b>					
Dy1—N4	2.498 (3)	Dy1—O1	2.209 (3)	Dy1—N3	2.536 (3)
Dy1—N1	2.542 (3)	Dy1—O3	2.192 (3)	Dy1—O2	2.203 (3)
Dy1—N2	2.498 (4)				
<b>Bond angles (°)</b>					
N4—Dy1—N3	73.58 (10)	N4—Dy1—N1	82.67 (10)	O1—Dy1—N4	94.51 (10)
O1—Dy1—N3	77.64 (10)	O1—Dy1—N1	72.24 (10)	O1—Dy1—N2	97.57 (16)
N3—Dy1—N1	139.73 (10)	O3—Dy1—N4	73.50 (10)	O3—Dy1—O1	157.21 (11)
O3—Dy1—N3	115.78 (10)	O3—Dy1—N1	86.80 (11)	O3—Dy1—O2	92.84 (12)
O3—Dy1—N2	82.98 (15)	O2—Dy1—N4	133.02 (10)	O2—Dy1—O1	109.18 (12)
O2—Dy1—N3	72.85 (10)	O2—Dy1—N1	142.51 (10)	O2—Dy1—N2	73.00 (12)

N2—Dy1—N4	144.62 (12)	N2—Dy1—N3	141.56 (12)	N2—Dy1—N1	69.75 (13)
<b>3</b>					
<b>Bond lengths (Å)</b>					
Dy1—O1	2.207 (3)	Dy1—O3	2.190 (3)	Dy1—O2	2.201 (3)
Dy1—N4	2.495 (3)	Dy1—N1	2.527 (4)	Dy1—N3	2.517 (4)
Dy1—N2	2.503 (5)				
<b>Bond angles (°)</b>					
O1—Dy1—N4	94.20 (12)	O1—Dy1—N1	72.35 (12)	O1—Dy1—N3	77.89 (12)
O1—Dy1—N2	97.46 (19)	O3—Dy1—O1	157.28 (12)	O3—Dy1—O2	93.06 (13)
O3—Dy1—N4	73.41 (11)	O3—Dy1—N1	87.04 (12)	O3—Dy1—N3	115.03 (12)
O3—Dy1—N2	83.79 (17)	O2—Dy1—O1	109.01 (13)	O2—Dy1—N4	133.28 (12)
O2—Dy1—N1	141.95 (12)	O2—Dy1—N3	72.86 (12)	O2—Dy1—N2	72.46 (15)
N4—Dy1—N1	83.06 (12)	N4—Dy1—N3	73.31 (11)	N4—Dy1—N2	145.30 (13)
N3—Dy1—N1	140.22 (12)	N2—Dy1—N1	69.73 (15)	N2—Dy1—N3	141.16 (13)
<b>4</b>					
<b>Bond lengths (Å)</b>					
Dy1—O1	2.185 (3)	Dy1—O3	2.187 (3)	Dy1—O2	2.200 (3)
Dy1—N1	2.530 (4)	Dy1—N4	2.482 (4)	Dy1—N3	2.504 (4)
Dy1—N2	2.503 (4)				
<b>Bond angles (°)</b>					
O1—Dy1—O3	159.45 (13)	O1—Dy1—O2	108.16 (13)	O1—Dy1—N1	73.07 (12)
O1—Dy1—N4	92.33 (13)	O1—Dy1—N3	79.22 (12)	O1—Dy1—N2	92.67 (14)
O3—Dy1—O2	91.99 (13)	O3—Dy1—N1	88.64 (13)	O3—Dy1—N4	74.63 (13)
O3—Dy1—N3	111.37 (12)	O3—Dy1—N2	88.98 (14)	O2—Dy1—N1	142.16 (12)
O2—Dy1—N4	137.41 (12)	O2—Dy1—N3	73.47 (12)	O2—Dy1—N2	74.01 (13)
N4—Dy1—N1	78.91 (12)	N4—Dy1—N3	74.39 (12)	N4—Dy1—N2	143.54 (13)
N3—Dy1—N1	140.33 (13)	N2—Dy1—N1	68.17 (13)	N2—Dy1—N3	141.93 (13)
<b>5</b>					
<b>Bond lengths (Å)</b>					

Dy1—O3	2.197 (2)	Dy1—O1	2.197 (3)	Dy1—O2	2.187 (2)
Dy1—N4	2.487 (3)	Dy1—N3	2.532 (3)	Dy1—N1	2.512 (3)
Dy1—N2	2.509 (3)				
<b>Bond angles (°)</b>					
O3—Dy1—O1	162.12 (9)	O3—Dy1—N4	73.03 (9)	O3—Dy1—N3	112.56 (9)
O3—Dy1—N1	89.80 (9)	O3—Dy1—N2	84.90 (9)	O1—Dy1—N4	98.15 (9)
O1—Dy1—N3	78.45 (9)	O1—Dy1—N1	73.10 (9)	O1—Dy1—N2	93.57 (10)
O2—Dy1—O3	90.81 (10)	O2—Dy1—O1	106.13 (10)	O2—Dy1—N4	133.88 (9)
O2—Dy1—N3	73.96 (9)	N4—Dy1—N1	79.60 (8)	N4—Dy1—N2	141.63 (9)
N1—Dy1—N3	137.08 (9)	N2—Dy1—N3	145.01 (9)	N2—Dy1—N1	69.12 (8)

**Table S4.** Selected bond lengths (Å) and angles (°) of complex **1a**.

1a					
<b>Bond lengths (Å)</b>					
Dy1—O3	2.184 (2)	Dy1—O1	2.211 (2)	Dy1—O2	2.218 (2)
Dy1—N1	2.493 (2)	Dy1—N2	2.513 (2)	Dy1—N3	2.487 (2)
Dy1—N4	2.497 (2)				
<b>Bond angles (°)</b>					
O3—Dy1—O1	163.74 (8)	O3—Dy1—O2	90.42 (8)	O3—Dy1—N1	87.40 (8)
O3—Dy1—N2	92.72 (8)	O3—Dy1—N3	73.53 (8)	O1—Dy1—O2	105.76 (8)
O1—Dy1—N1	94.92 (8)	O1—Dy1—N2	73.26 (8)	O1—Dy1—N3	95.20 (8)
O1—Dy1—N4	80.65 (8)	O2—Dy1—N1	75.91 (8)	O2—Dy1—N2	144.51 (7)
O2—Dy1—N3	135.59 (8)	O2—Dy1—N4	73.57 (8)	N1—Dy1—N2	68.94 (8)
N3—Dy1—N1	141.53 (9)	N3—Dy1—N2	78.73 (7)	N3—Dy1—N4	71.82 (8)
N4—Dy1—N2	138.33(8)				

**Table S5.** *SHAPE* analysis of the Dy<sup>III</sup> ion in **1**.

Label	Shape	Symmetry	Distortion(°)
HP-7	$D_{7h}$	Heptagon	33.364
HPY-7	$C_{6v}$	Hexagonal pyramid	21.488

PBPY-7	$D_{5h}$	Pentagonal bipyramid	2.719
COC-7	$C_{3v}$	Capped octahedron	4.237
CTPR-7	$C_{2v}$	Capped trigonal prism	3.779
JPBPY-7	$D_{5h}$	Johnson pentagonal bipyramid J13	4.577
JETPY-7	$C_{3v}$	Johnson elongated triangular pyramid J7	17.181

**Table S6.** *SHAPE* analysis of the Dy<sup>III</sup> ion in 2.

Label	Shape	Symmetry	Distortion(°)
HP-7	$D_{7h}$	Heptagon	32.933
HPY-7	$C_{6v}$	Hexagonal pyramid	21.101
PBPY-7	$D_{5h}$	Pentagonal bipyramid	4.156
COC-7	$C_{3v}$	Capped octahedron	3.488
CTPR-7	$C_{2v}$	Capped trigonal prism	3.026
JPBPY-7	$D_{5h}$	Johnson pentagonal bipyramid J13	5.844
JETPY-7	$C_{3v}$	Johnson elongated triangular pyramid J7	14.361

**Table S7.** *SHAPE* analysis of the Dy<sup>III</sup> ion in 3.

Label	Shape	Symmetry	Distortion(°)
HP-7	$D_{7h}$	Heptagon	33.055
HPY-7	$C_{6v}$	Hexagonal pyramid	21.420
PBPY-7	$D_{5h}$	Pentagonal bipyramid	4.052
COC-7	$C_{3v}$	Capped octahedron	3.600
CTPR-7	$C_{2v}$	Capped trigonal prism	3.043
JPBPY-7	$D_{5h}$	Johnson pentagonal bipyramid J13	5.766
JETPY-7	$C_{3v}$	Johnson elongated triangular pyramid J7	14.476

**Table S8.** *SHAPE* analysis of the Dy<sup>III</sup> ion in 4.

Label	Shape	Symmetry	Distortion(°)
HP-7	$D_{7h}$	Heptagon	33.539
HPY-7	$C_{6v}$	Hexagonal pyramid	21.933
PBPY-7	$D_{5h}$	Pentagonal bipyramid	3.072

COC-7	$C_{3v}$	Capped octahedron	3.851
CTPR-7	$C_{2v}$	Capped trigonal prism	2.891
JPBPY-7	$D_{5h}$	Johnson pentagonal bipyramid J13	4.753
JETPY-7	$C_{3v}$	Johnson elongated triangular pyramid J7	16.678

**Table S9.** *SHAPE* analysis of the Dy<sup>III</sup> ion in **5**.

Label	Shape	Symmetry	Distortion(°)
HP-7	$D_{7h}$	Heptagon	34.012
HPY-7	$C_{6v}$	Hexagonal pyramid	20.859
PBPY-7	$D_{5h}$	Pentagonal bipyramid	3.536
COC-7	$C_{3v}$	Capped octahedron	3.293
CTPR-7	$C_{2v}$	Capped trigonal prism	3.076
JPBPY-7	$D_{5h}$	Johnson pentagonal bipyramid J13	5.407
JETPY-7	$C_{3v}$	Johnson elongated triangular pyramid J7	15.984

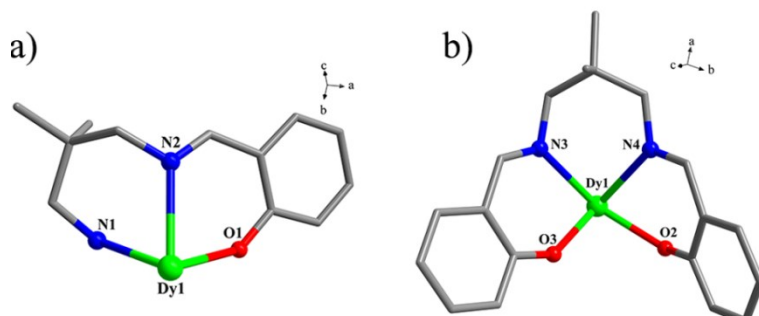


**Figure S1.** Two different coordination modes of Schiff base ligand in the independent unit of **1**, a) coordination mode of  $\text{HL}^{1-\text{H}}$ , b) coordination mode of  $\text{H}_2\text{L}^{1-\text{H}}$ .

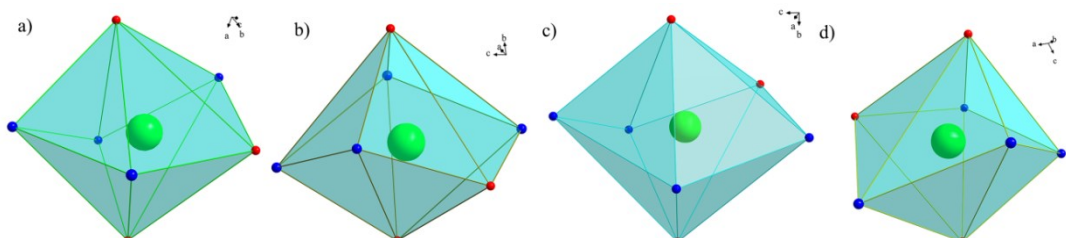


**Figure S2.** The coordination polyhedrons around Dy(III) ions in complexes **2–5**, a–d correspond to complexes **2–5**, respectively.

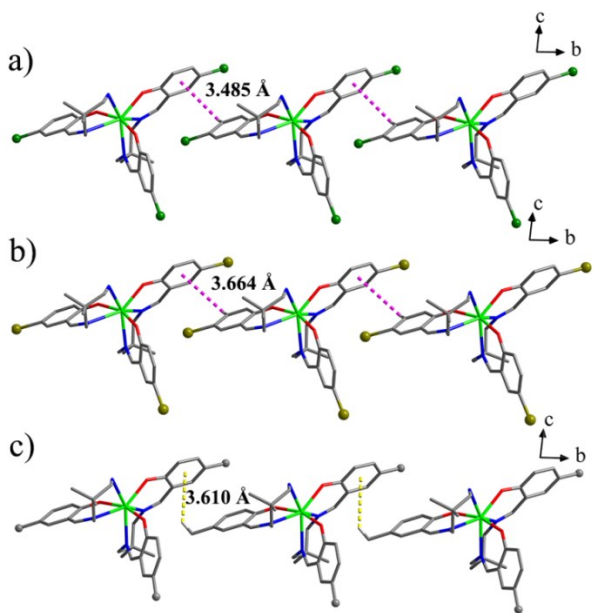


**Figure S3.** a) Weak interaction of C–H $\cdots$  $\pi$  (Ph) between molecules at a direction, a) for **2**, b) for **3**, c) for **4**.

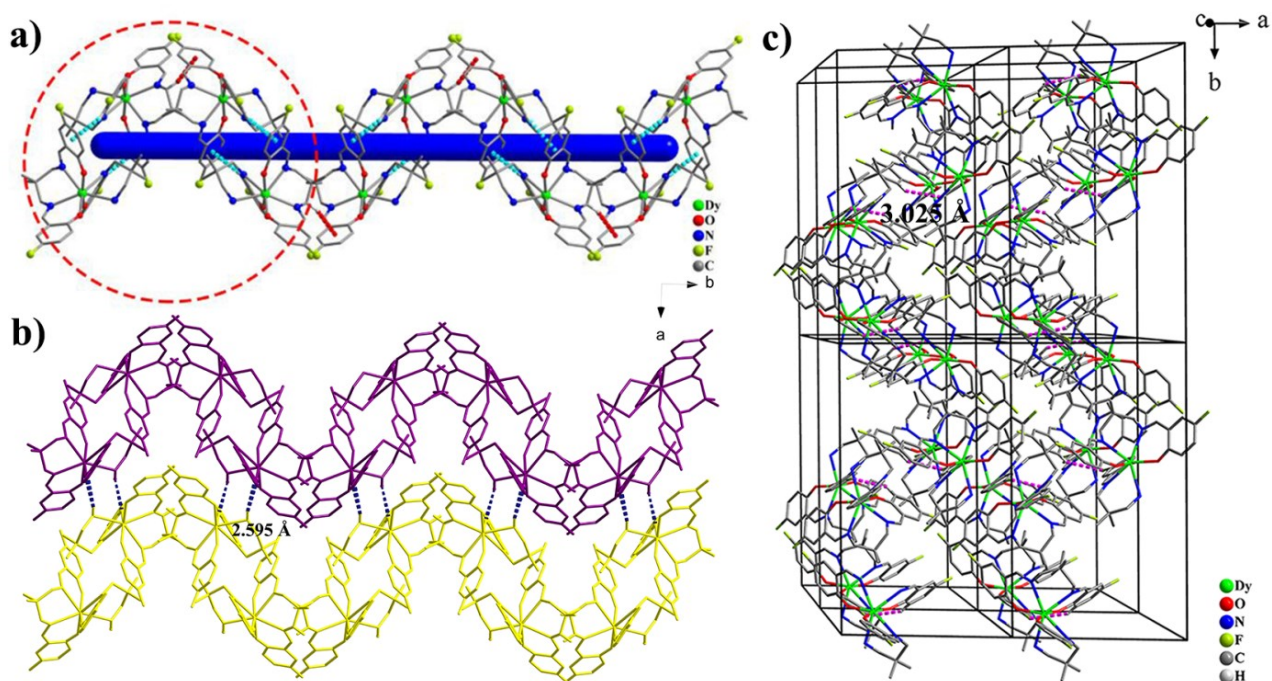


**Figure S4.** Crystal structure of **5**, a) 1D chain; b) 2D layer; c) 3D supramolecular framework.

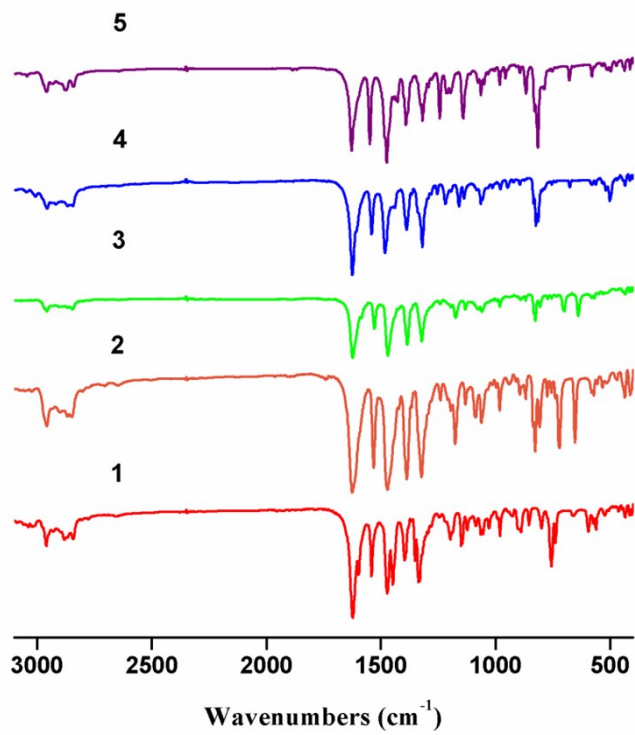


**Figure S5.** IR spectra of **1** (red), **2** (brown), **3** (green), **4** (blue), and **5** (purple).

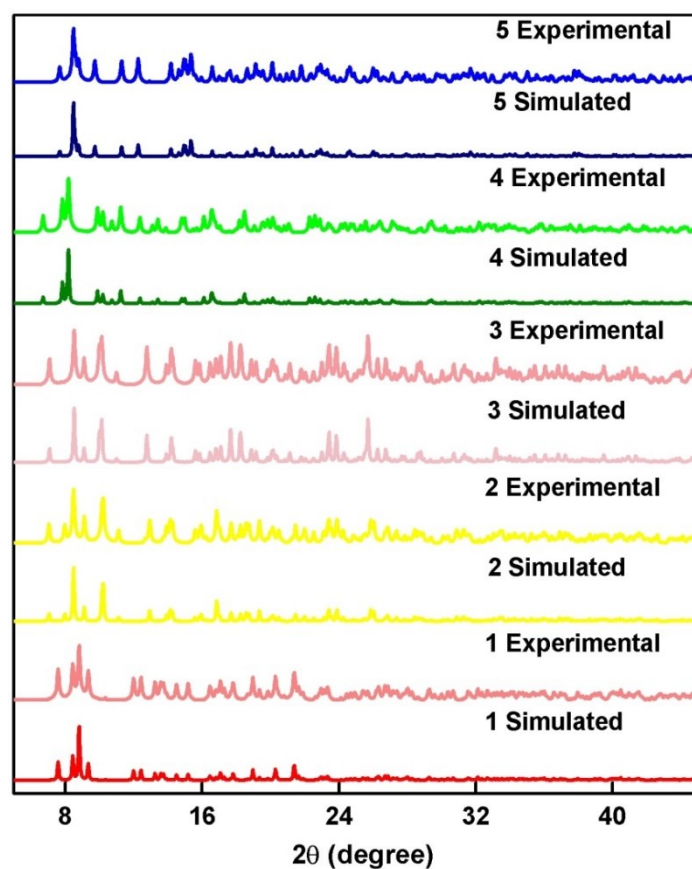


**Figure S6.** Theoretical and experimental PXRD patterns of **1–5**.

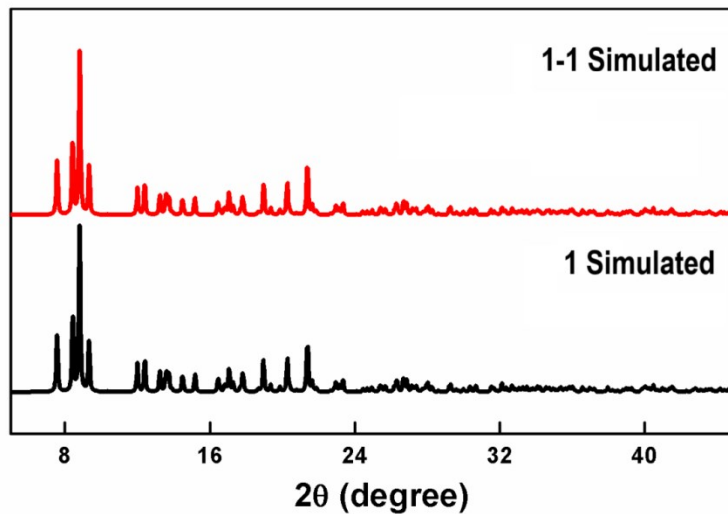


**Figure S7.** Theoretical PXRD patterns of **1** and **1a**.

### Thermal analysis.

The thermal stability of **1–5** were tested in the temperature range of 35–1000 °C with a N<sub>2</sub> flow rate of 5 °C/min. The DTG and TG curves show that these Dy–HOFs exhibit similar weight loss behaviors, and they are very stable and began to show the first weight loss at about 300 °C, which were attributed to the structural collapse of these compounds (Figure S7).

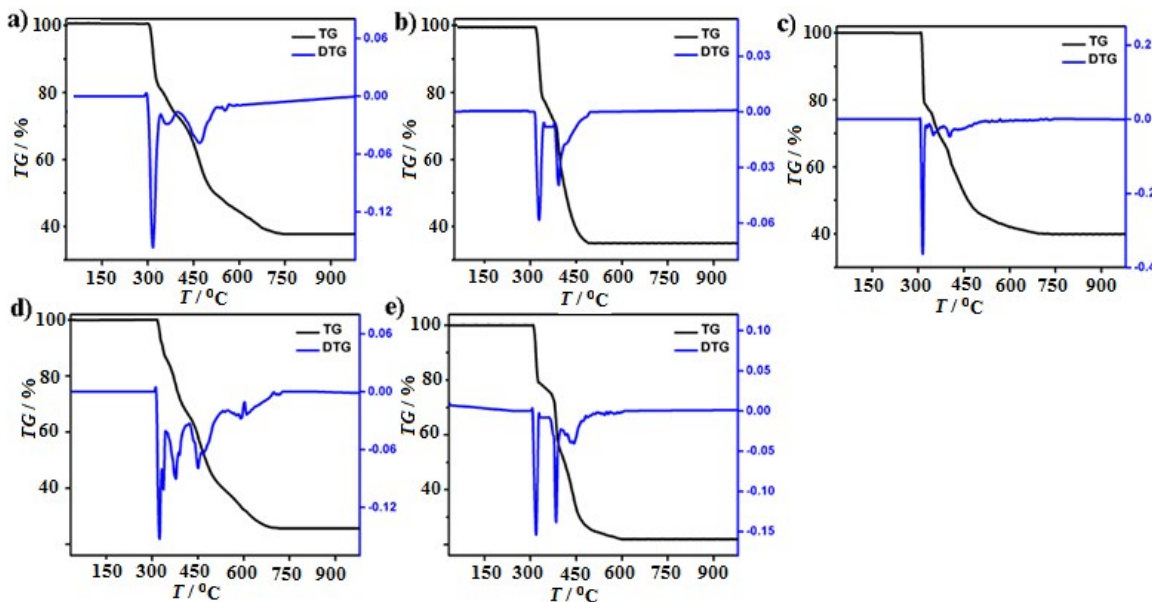


**Figure S8.** Thermogravimetric curves of complexes **1–5** (a–e, TG and DTG).

**1** was soaked in methanol, ethanol and acetonitrile for 6 hours and then dried naturally for thermogravimetric test. The results showed that **1** soaked in methanol has a weight loss of 3.18% before 90 °C and this corresponds to the loss of two methanol molecules in each hole in the DyHOF.

Similarly, **1** soaked in ethanol lost 3 ethanol molecules before 90 °C, and when soaked in acetonitrile lost 2 acetonitrile molecules before 90 °C.

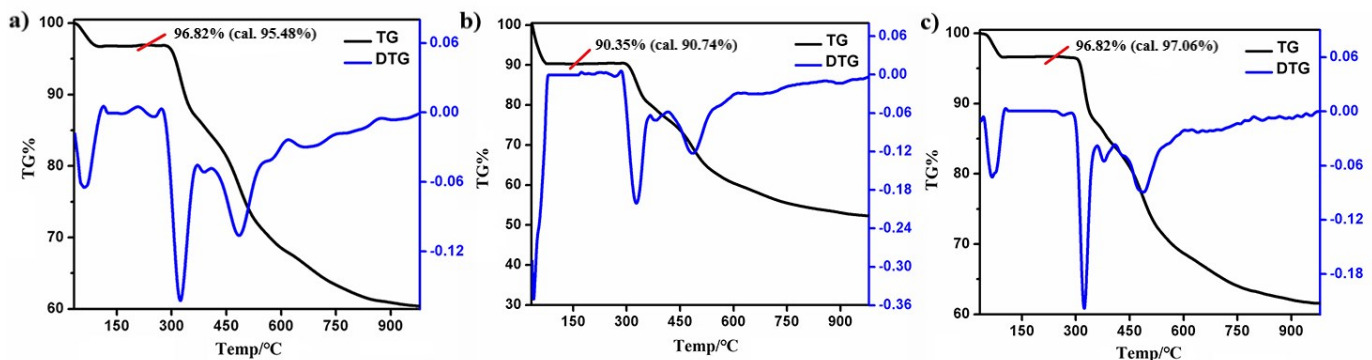


**Figure S9.** Thermogravimetric curve of solvent exchange for complex **1** (a for  $\text{CH}_3\text{OH}$ , b for  $\text{C}_2\text{H}_5\text{OH}$ , c for  $\text{CH}_3\text{CN}$ )

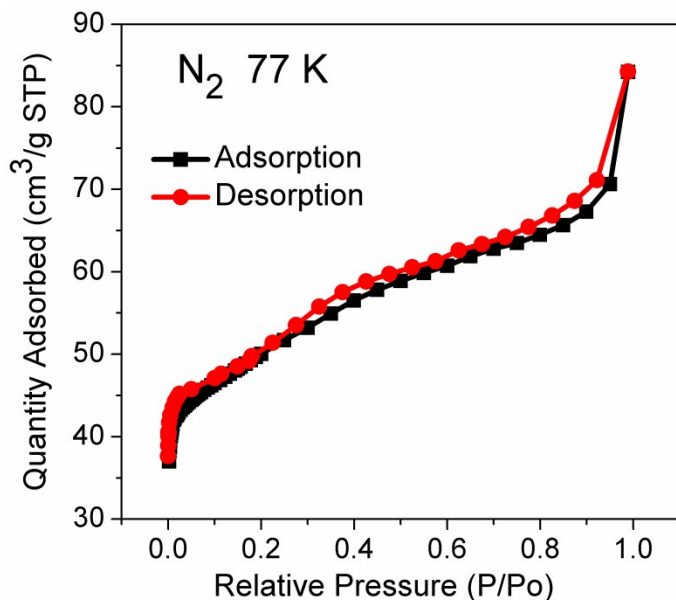


**Figure S10.**  $\text{N}_2$  adsorption and desorption isotherms of **1** at 77 K.

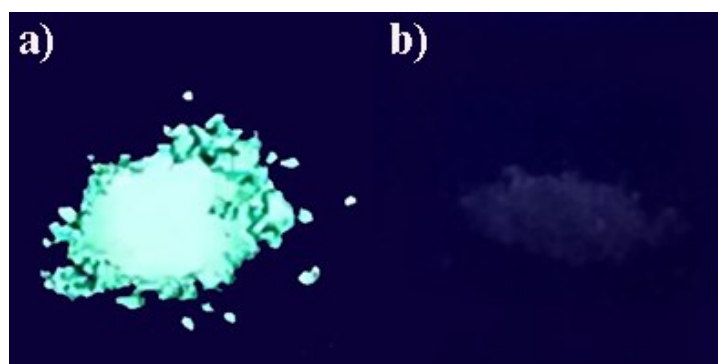


**Figure S11.** Photos of the sample **1** immersed in HCl aqueous solution (a) and original sample (b)

seen under the radiation of 365 nm UV lamp.

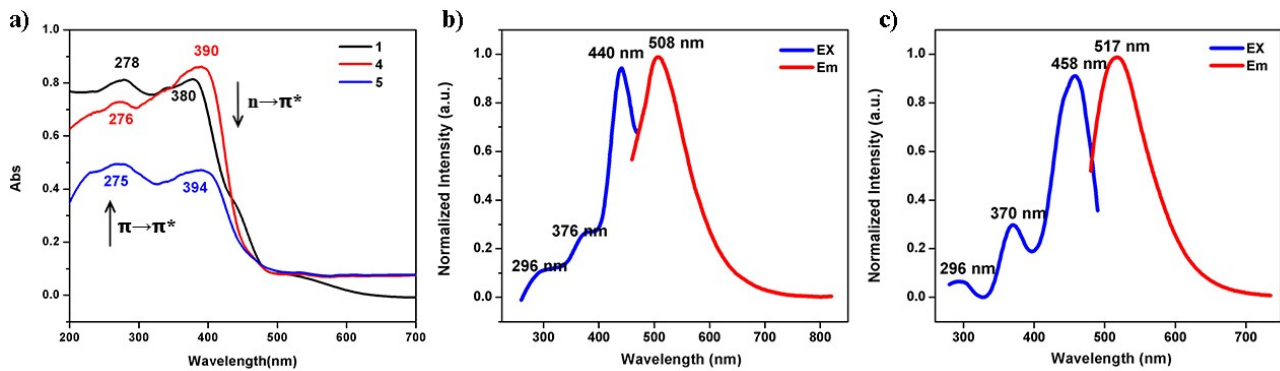


**Figure S12.** (a) The UV-Vis absorption spectra of **1**, **4** and **5**; Solid-state fluorescence of complexes **4** (b) and **5** (c).

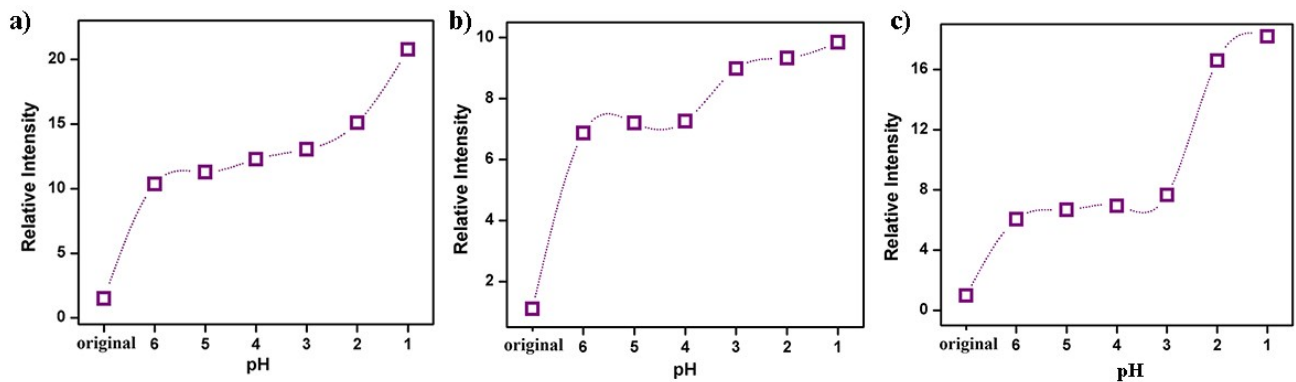


**Figure S13.** The pH stimuli-response luminescence intensity with a)  $\lambda_{\text{ex}} = 429$  nm for **1**, b)  $\lambda_{\text{ex}} = 440$  nm for **4**, c)  $\lambda_{\text{ex}} = 458$  nm for **5**.

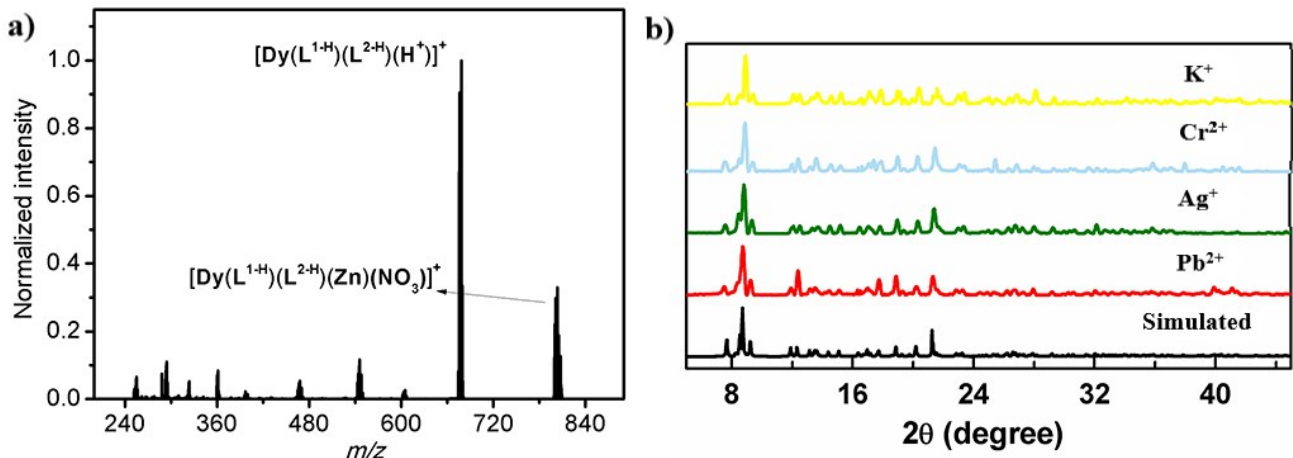


**Figure S14.** a) Mass spectrometry analysis of the sample **1a** responding to  $Zn^{2+}$ ; b) Theoretical and experimental PXRD patterns of the sample **1a** responding to metal ions.

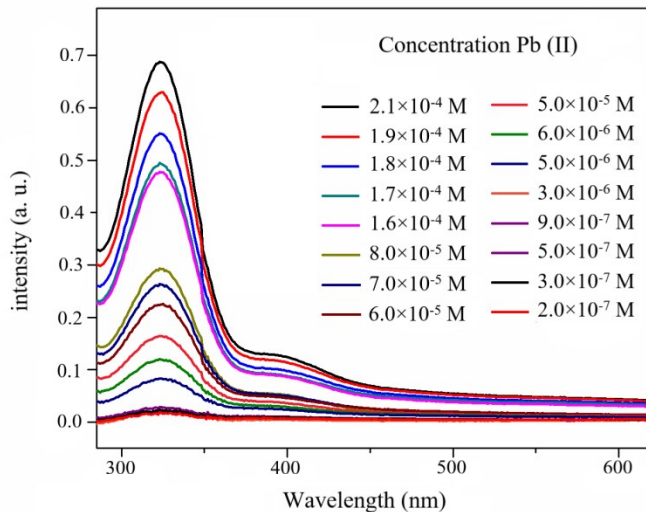


**Figure S15.** UV absorption of sample **1a** to aqueous solutions containing Pb(II) ions of different concentrations.

**Table S10.** Operating conditions for elemental analysis to use ICP-OES.

parameters	value
Radio frequency power	1250 w
Plasma flow	15 L min <sup>-1</sup>
Auxiliary flow	1.5 L min <sup>-1</sup>
Nebulizer flow	0.75 L min <sup>-1</sup>
Replicate read time	1.0 s
Pump rate	15 rpm
Instr stabilization delay	15 s
Sample uptake delay	15 s
Rinse time	25 s

**Table S11.** Analytical features of ICP-OES to determine whether Pb(II) ions are entered in the **1a** frame in response to Pb(II) ions.

element	Sample weight (g)	Constant volume (mL)	Solution element content (mg/L)	Sample element content (%)
Dy	0.0202	10	2.11	10.45
Pb	0.0202	10	0.64	0.03

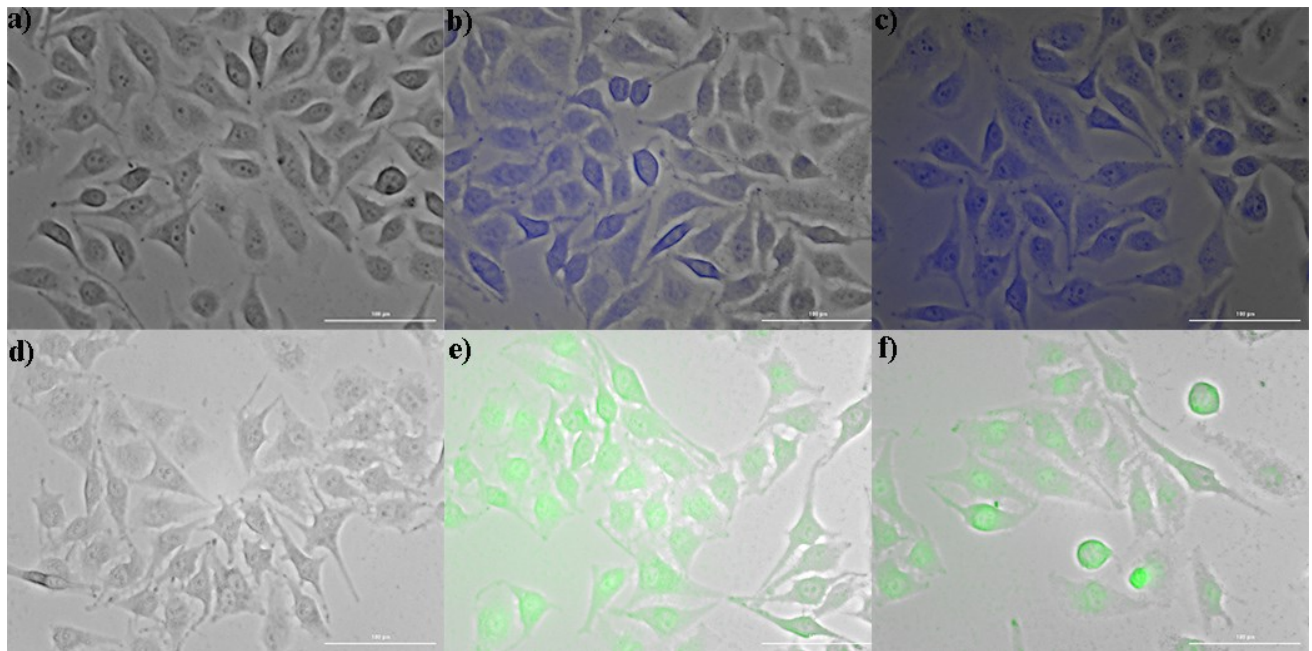


**Figure S16.** *HeLa* cells without wavelength excitation as a control group (a for **1**, d for **5**); At 429 nm, the state of *HeLa* cells after adding original non-luminescent sample **1** (b), and sample **1** which was soaked in HCl (c); At 458 nm, the state of *HeLa* cells after adding original non-luminescent sample sample **5** (e), and sample **5** which was soaked in HCl (f) (scale: 100  $\mu$ m).

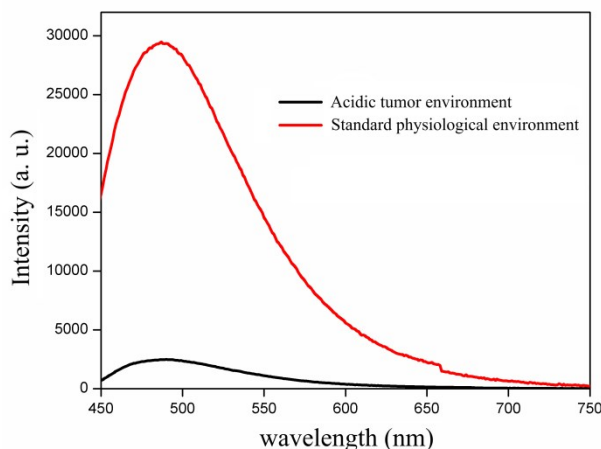


**Figure S17.** Fluorescence of the DMSO solution of **1** in a simulated environment.

### Magnetic properties.

Under the applied DC field of 1000 Oe, the magnetic susceptibilities of the series of Dy–HOFs were measured in the temperature range 2–300 K. As show in Figure S18, the values of the  $\chi_M T$  at 300 K for **1-5** are 13.56, 15.35, 13.68, 14.03, and 15.31  $\text{cm}^3 \text{K mol}^{-1}$  respectively, which are close to the expected value ( $14.17 \text{ cm}^3 \text{K mol}^{-1}$ ) for a free Dy(III) ion ( ${}^6\text{H}_{15/2}$ ,  $g = 4/3$ ).<sup>1-3</sup> At high temperatures, the  $\chi_M T$  values are change slowly and then undergo a quick decrease upon cooling,

reach a minimum values at 2 K (9.37, 13.78, 12.33, 12.13 and 11.50 cm<sup>3</sup> K mol<sup>-1</sup> for **1-5**, respectively). The decline of the  $\chi_M T$  with a lowering temperature may cause by the thermal depopulation of the stark sublevels of the Dy(III) ion.<sup>4-5</sup>

The isothermal magnetization ( $M$ ) of these Dy–HOFs was measured in a field range of 0-50 kOe at different temperatures (Figure S19). It can be seen from the plots that the  $M$ – $H$  curves do not overlap and tend to saturate after reaching the high field area and the maximum magnetization are 8.96  $N\mu_B$ , 6.46  $N\mu_B$ , 6.29  $N\mu_B$ , 8.06  $N\mu_B$ , 7.16  $N\mu_B$  at 2 K and 50 kOe, respectively. Compared with the expected saturation value of 10  $N\mu_B$  for one non-interacting Dy(III) ion, the above  $M$  values are all slightly smaller but close to it.<sup>6,7</sup> This can be attributed to the quenching of the ground state degenerate state which caused by the magnetic anisotropy and crystal field effect.<sup>8,9</sup>

To further explore the original slow magnetic relaxation behaviors of the **1-5**, Cole–Cole plots under 0 DC field were fitted to the generalized Debye model.<sup>10,11</sup> As shown in Figure S22, all of the complexes show a relatively symmetrical semicircle shapes except **2** and **3**. The difference probable is the result of the substitution effect. The  $\ln(\tau/\text{s})$  versus  $T^{-1}$  curves for these **Dy–HOFs** are also plotted (Figure S23). The relaxation time in the high temperature region can be well described by a single thermodynamic process: i.e., an Orbach process following the Arrhenius law  $\ln(\tau) = T^{-1} \cdot U_{\text{eff}}/k_B + \ln(\tau_0)$ .<sup>12</sup> The high temperature area of  $\ln(\tau/\text{s})$  versus  $T^{-1}$  is indicative of a dominant Orbach relaxation mechanism, the effective energy barrier  $U_{\text{eff}}$  and relaxation time  $\tau_0$  are 2.28 K,  $1.19 \times 10^{-3}$  s for **1**, 2.99 K,  $8.99 \times 10^{-4}$  s for **2**, 1.21 K,  $1.11 \times 10^{-5}$  s for **3**, 0.60 K,  $3.08 \times 10^{-4}$  s for **4**, and 1.06 K,  $6.05 \times 10^{-4}$  s for **5**. However, the  $\ln(\tau)$  vs.  $T^{-1}$  plots are gradually curved in the low temperature range. Therefore, in order to adapt to a larger temperature range, the fitting process should include multiple relaxation processes. Therefore, the Raman, Orbach and QTM mechanisms are applied to fit the whole  $\ln(\tau)$  vs.  $T^{-1}$  plots:  $\tau^{-1} = \tau_0^{-1} \exp(T^{-1} \cdot U_{\text{eff}}/k_B) + CT^n$ .<sup>11</sup> The  $U_{\text{eff}}$  and  $\tau_0$  are, 15.58 K,  $5.27 \times 10^{-4}$  s for **1**, 9.71 K,  $3.62 \times 10^{-6}$  s for **2**, 3.53 K,  $2.04 \times 10^{-4}$  s for **3**, 17.99 K,  $1.19 \times 10^{-4}$  s for **4**, 25.31 K,  $8.87 \times 10^{-5}$  s for **5** (Figure S23) respectively. In summary, considering a more reasonable fitting method, the order of the  $U_{\text{eff}}$  can be obtained as **5** (F) > **4** (Me) > **1** (H) > **2** (Cl) > **1** (Br), which mainly caused by the changes of substituents.

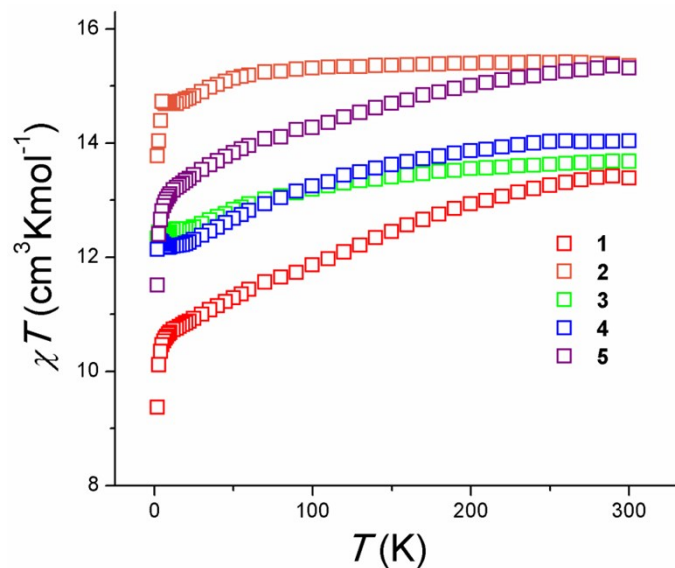


**Figure S18.** Temperature dependence of  $\chi_M T$  for **1–5**.

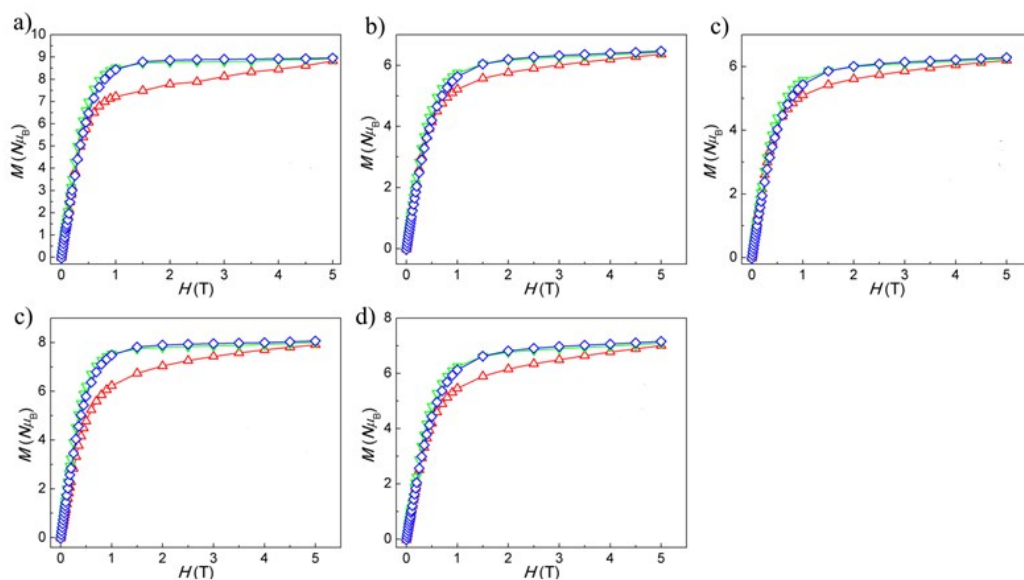


**Figure S19.**  $M$  vs.  $H$  plots for **1** (a), **2** (b), **3** (e), **4** (c), **5** (d). 2 K, green line; 2.5 K, blue line; 3 K, red line.

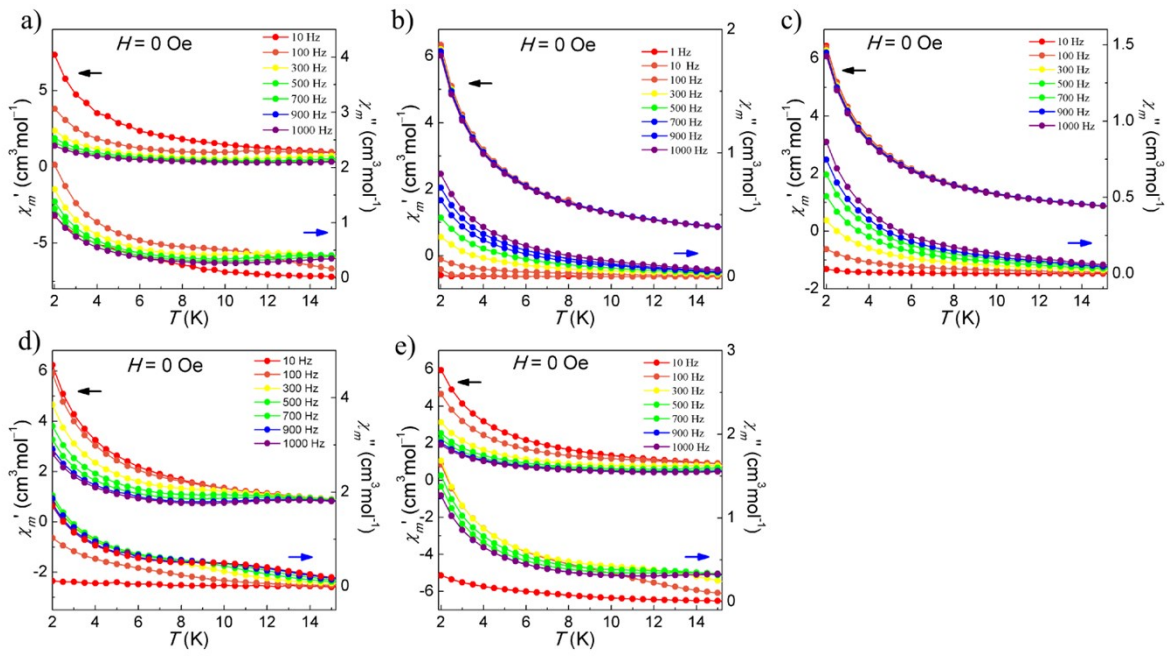


**Figure S20.** Temperature-dependent  $\chi'$  and  $\chi''$  AC susceptibilities under 0 DC fields for **1** (a), **2** (b), **3** (c), **4** (d), and **5** (e).

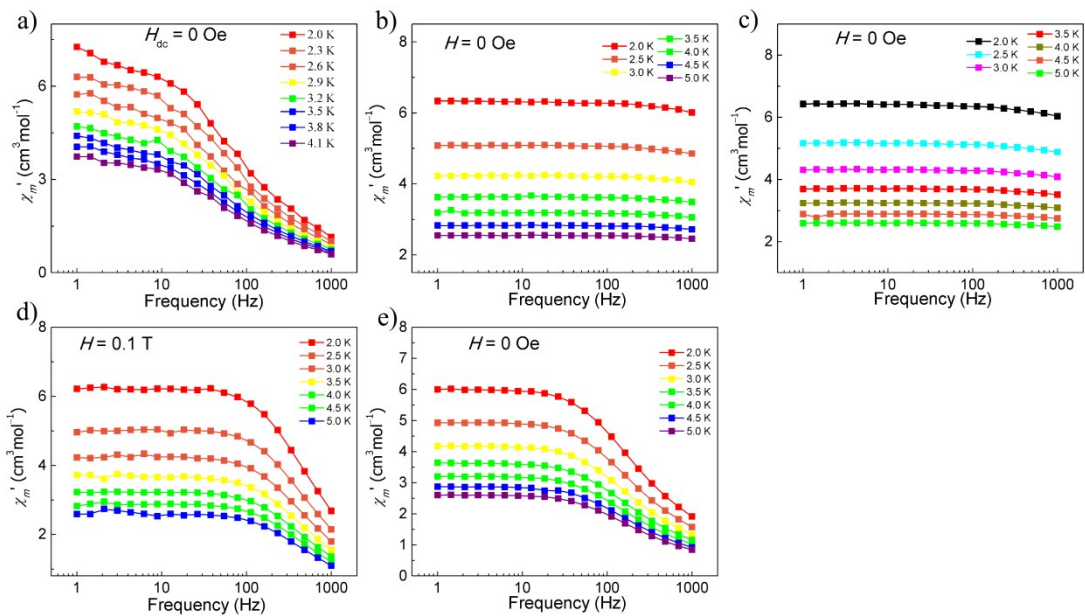


**Figure S21.** In-phase ( $\chi'$ ) magnetic susceptibility vs frequency under 0 DC field for **1** (a), **2** (b), **3** (c), **4** (d), and **5** (e).

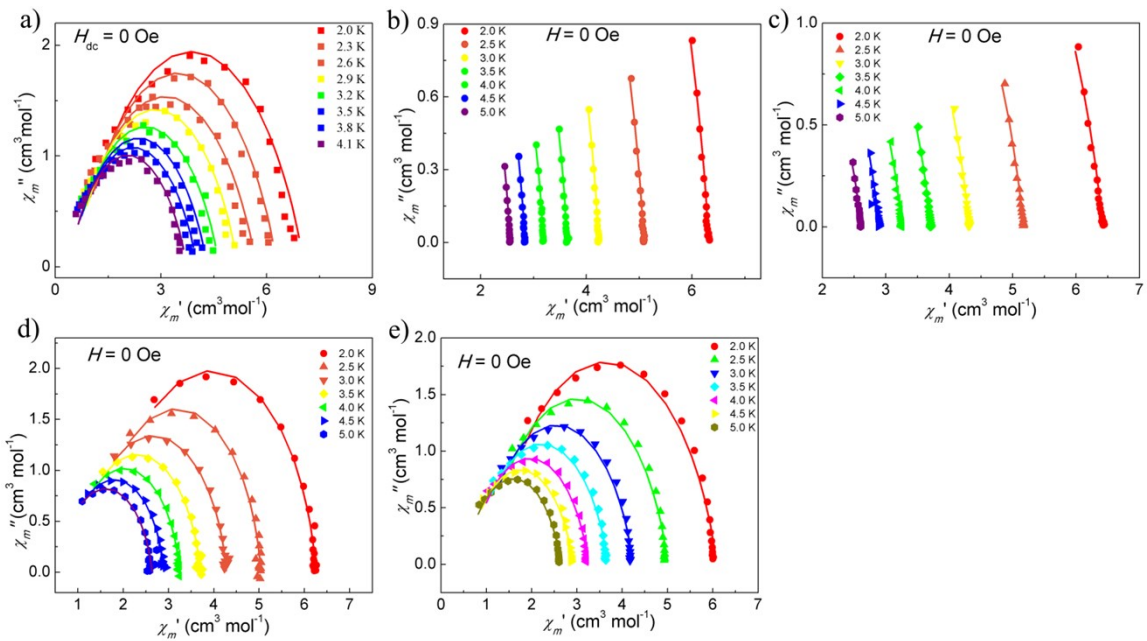


**Figure S22.** Cole-Cole plots for **1** (a), **2** (b), **3** (c), **4** (d), and **5** (e), solid lines are the best fits to the Debye model.

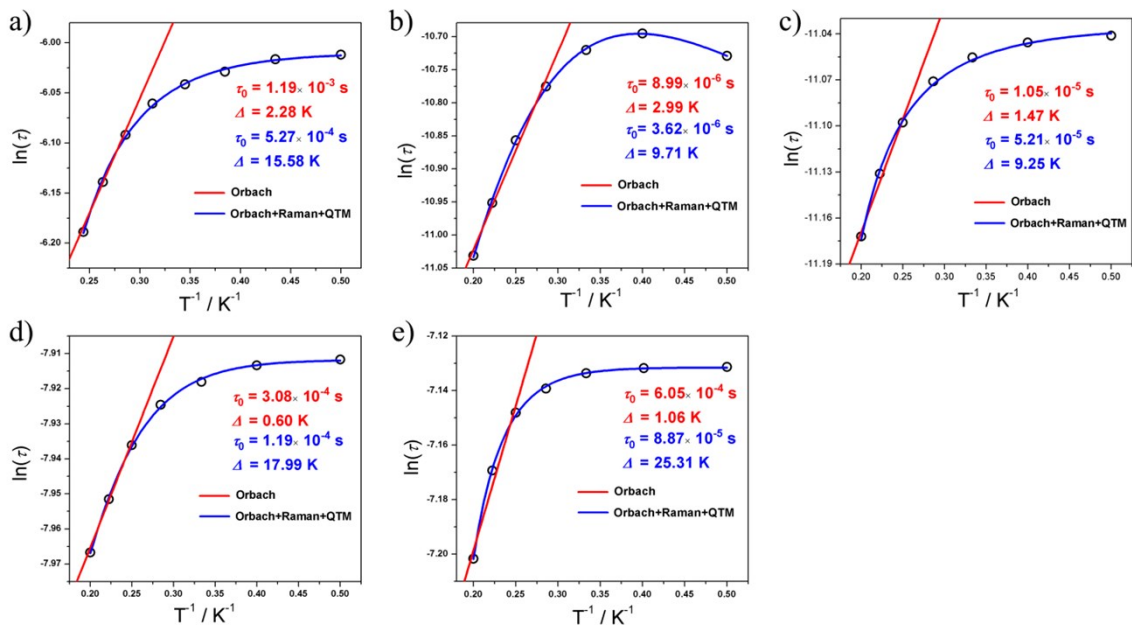


**Figure S23.**  $\ln(\tau)$  vs.  $T^{-1}$  plots for **1** (a), **2** (b), **3** (c), **4** (d), and **5** (e), the solid lines show the best fits with the Arrhenius formula (linear) and the multiple relaxation processes equation (curve).

**Table S12.** Selected parameters from the fitting result of the Cole–Cole plots for **1** under 0 Oe field.

	<b>1</b>		
Temp.(K)	$\tau$	$\alpha$	residual

2.0	0.2471E-02	0.3122	0.1728
2.3	0.2458E-02	0.3200	0.2347
2.6	0.2370E-02	0.3158	0.2432
2.9	0.2270E-02	0.3112	0.2693
3.2	0.2300E-02	0.3033	0.2586
3.5	0.2271E-02	0.3182	0.4289
3.8	0.2157E-02	0.2952	0.3650
4.1	0.2052E-02	0.3048	0.5786

**Table S13.** Selected parameters from the fitting result of the Cole–Cole plots for **2** and **3** under 0 Oe field.

Temp.(K)	<b>2</b>			<b>3</b>		
	$\tau$	$\alpha$	residual	$\tau$	$\alpha$	residual
2.0	0.1597E-04	0.1234	0.4426E-03	0.1575E-04	0.2068	0.9115E-02
2.5	0.1624E-04	0.1278	0.9844E-03	0.1594E-04	0.1959	0.4550E-02
3.0	0.1636E-4	0.1302	0.2002E-01	0.1590E-04	0.1875	0.3236E-02
3.5	0.1654E-4	0.1333	0.2648E-02	0.1564E-04	0.1877	0.2098E-02
4.0	0.1665E-4	0.1353	0.17268E-02	0.1511E-04	0.1857	0.1662E-02
4.5	0.1668E-4	0.1513	0.29288E-02	0.1548E-04	0.1655	0.2722E-02
5.0	0.1619E-4	0.1623	0.5395E-02	0.1406E-04	0.1855	0.1051E-02

**Table S14.** Selected parameters from the fitting result of the Cole–Cole plots for **4** and **5** under 0 Oe field.

Temp.(K)	<b>4</b>			<b>5</b>		
	$\tau$	$\alpha$	residual	$\tau$	$\alpha$	residual
2.0	0.3562E-03	0.1365	0.8361E-01	0.7935E-03	0.2036	0.2635 E-01
2.5	0.3621E-03	0.1180	0.3149E-01	0.7922E-03	0.2067	0.3413E-01
3.0	0.3646E-03	0.1121	0.1892E-01	0.7977E-03	0.2020	0.4195E-01
3.5	0.3627E-03	0.1173	0.5021E-01	0.7933E-03	0.2032	0.5396E-01
4.0	0.3576E-03	0.1166	0.4424E-01	0.7863E-03	0.1987	0.7243E-01

4.5	0.3566E-03	0.8958E-01	0.5453E-01	0.7698E-03	0.1958	0.1018
5.0	0.3468E-03	0.9886E-01	0.4756E-01	0.7453E-03	0.1960	0.1423

## References

- (1) Liu, J.; Chen, Y. C.; Liu, J. L.; Vieru, V.; Ungur, L.; Jia, J. H.; Chibotaru, L. F.; Lan, Y.; Wernsdorfer, W.; Gao, S.; Chen, X. M.; Tong, M. L. A Stable Pentagonal Bipyramidal Dy(III) Single-Ion Magnet with a Record Magnetization Reversal Barrier over 1000 K. *J. Am. Chem. Soc.* **2016**, *138*, 5441–5450.
- (2) Chen, Y. C.; Liu, J. L.; Ungur, L.; Liu, J.; Li, Q. W.; Wang, L. F.; Ni, Z. P.; Chibotaru, L. F.; Chen X. M.; Tong, M. L.; Symmetry-Supported Magnetic Blocking at 20 K in Pentagonal Bipyramidal Dy(III) Single-Ion Magnets. *J. Am. Chem. Soc.* **2016**, *138*, 2829–2837.
- (3) Jiang, Z.; Sun, L.; Yang, Q.; Yin, B.; Ke, H.; Han, J.; Wei, Q.; Xie, G.; Chen, S. P. Excess axial electrostatic repulsion as a criterion for pentagonal bipyramidal Dy<sup>III</sup> single-ion magnets with high  $U_{\text{eff}}$  and  $T_B$ . *J. Mater. Chem. C.* **2018**, *6*, 4273–4280.
- (4) Wu, J.; Cador, O.; Li, X. L.; Zhao, L.; Guennic, B. Le.; Tang, J. Axial Ligand Field in  $D_{4d}$  Coordination Symmetry: Magnetic Relaxation of Dy SMMs Perturbed by Counteranions. *Inorg. Chem.* **2017**, *56*, 11211–11219.
- (5) Fondo, M.; Corredoira-Vázquez, J.; García-Deibe, A. M.; Sanmartín-Matalobos, J.; Herrera, J. M.; Colacio, E. Designing Ligands to Isolate ZnLn and Zn<sub>2</sub>Ln Complexes: Field-Induced Single-Ion Magnet Behavior of the ZnDy, Zn<sub>2</sub>Dy, and Zn<sub>2</sub>Er Analogues. *Inorg. Chem.* **2017**, *56*, 5646–5656.
- (6) Tang, J. K.; Hewitt, I.; Madhu, N. T.; Chastanet, G.; Wernsdorfer, W.; Anson, C. E.; Benelli, C.; Sessoli, R.; Powell, A. K. Dysprosium Triangles Showing Single-Molecule Magnet Behavior of Thermally Excited Spin States. *Angew. Chem., Int. Ed.* **2006**, *45*, 1729–1733.
- (7) Liu, X. Y.; Ma, X. F.; Yuan, W. Z.; Cen, P. P.; Zhang, Y. Q.; FerrandoSoria, J.; Xie, G.; Chen, S. P.; Pardo, E. Concise Chemistry Modulation of the SMM Behavior within a Family of Mononuclear Dy(III) Complexes. *Inorg. Chem.* **2018**, *57*, 14843–14851.
- (8) Li, M.; Wu, H.; Yang, Q.; Ke, H.; Yin, B.; Shi, Q.; Wang, W.; Wei, Q.; Xie, G.; Chen, S. Experimental and Theoretical Interpretation on the Magnetic Behavior in a Series of Pentagonal-Bipyramidal Dy<sup>III</sup> Single-Ion Magnets. *Chem. Eur. J.* **2017**, *23*, 17775–17787.
- (9) Das, C.; Upadhyay, A.; Shanmugam, M. Influence of Radicals on Magnetization Relaxation Dynamics of Pseudo-Octahedral Lanthanide Iminopyridyl Complexes. *Inorg. Chem.* **2018**, *57*, 9002–9011.
- (10) Perfetti, M.; Gysler, M.; Rechkemmer-Patalen, Y.; Zhang, P.; Taştan, H.; Fischer, F.; Netz, J.; Frey, W.; Zimmermann, L. W.; Schleid, T.; Hakl, M.; Orlita, M.; Ungur, L.; Chibotaru, L.; Brock-Nannestad, T.; Piligkos, S.; Slageren, J. V. Determination of the electronic structure of a

- dinuclear dysprosium single molecule magnet without symmetry idealization. *Chem. Sci.* **2019**, *10*, 2101–2110.
- (11) Feng, M.; Ruan, Z. Y.; Chen, Y. C.; Tong, M. L. Physical stimulus and chemical modulations of bistable molecular magnetic materials. *Chem. Commun.* **2020**, *56*, 13702–13718.
- (12) Wang, H. L.; Ma, X. F.; Zhu, Z. H.; Zhang, Y. Q.; Zou, H. H.; Liang, F. P. A series of dysprosium-based hydrogen-bonded organic frameworks (Dy-HOFs): thermally triggered off→on conversion of a single-ion magnet. *Inorg. Chem. Front.* **2019**, *6*, 2906–2913.